









Observation of bulk-edge correspondence in topological pumping based on a tunable electric circuit

Kenichi Yatsugi ¹, Tsuneya Yoshida ², Tomonari Mizoguchi ², Yoshihito Kuno ², Hideo Iizuka ¹, Yukihiro Tadokoro ¹ & Yasuhiro Hatsugai ²

In topological phases, localized edge states protected by the bulk topological number appear. This phenomenon is known as the bulk-edge correspondence, which has been theoretically established in various topological systems including topological pumping. There have been experimental works on topological edge states. However, direct observation of bulk topological numbers remains challenging. Here, we experimentally observe both topological edge states and bulk Chern numbers near the topological phase transition in a tunable electric circuit system. The admittance matrix of the system is accurately engineered by using variable capacitors, leading to the implementation of classical analogue of the quantum Hall phase and the topological transition. The topological numbers of the edge states are determined experimentally, where the locations of the edge states are flipped in the topological transition. The corresponding bulk Chern numbers are determined by the Středa's formula to the impedance spectrum. Our electric circuit scheme is a promising platform to provide a crucial understanding of topological phenomena, and opens up the possibility toward functional energy transfer mechanisms.

¹Toyota Central R&D Labs., Inc., Nagakute, Aichi 480-1192, Japan. ²Department of Physics, University of Tsukuba, Tsukuba, Ibaraki 305-8571, Japan.
email: yatsugi@mosk.tytlabs.co.jp

Topological phases^{1–4} have localized edge states^{5,6} in the bulk band gap which are protected by non-trivial topological numbers. The quantum Hall effect⁷ is one of the celebrated examples of the topological phases of matter. The Hall conductance is given by the integer called the TKNN (Thouless-Kohmoto-Nightingale-den Nijs) integer defined for the bulk¹. The TKNN integer is a topological invariant which characterizes the topological aspects of the quantum Hall effect⁷, i.e., Chern number⁸. The important concept in such topological systems is the bulk-edge correspondence⁹. Although the bulk Chern number is not directly observed in general, the topological feature is captured by observing the edge states⁶.

The topology characterized by the Chern number also plays a crucial role in the particle transport called topological pumping in a periodic potential¹⁰. In the topological pumping, particles are pumped adiabatically by the cyclic modulation of the potential. The number of the pumped particles over each pumping cycle is equal to the sum of the Chern numbers of the filled bands. The topological pumping was recently realized in cold atom experiments^{11,12}. In these studies, the quantized particle transport in the bulk state was observed by the center of mass, and also it has been shown theoretically that the bulk-edge correspondence holds even in topological pumping¹³. Although the topological edge states have been experimentally observed in one-dimensional^{14–19} and higher-dimensional systems^{20–22}, including higher-order topological corner state^{23,24}, direct observation of the bulk Chern number and the experimental demonstration of bulk-edge correspondence in topological pumping are still challenging in real experimental systems because topological number is not a physical observable for the classical topological phases.

The topological phase transition is a phenomenon in which the Chern number changes accompanied by the gap-closing and -reopening²⁵. For tight-binding electrons on a square lattice with the nearest-neighbor (NN) and the next-nearest-neighbor (NNN) hoppings in a perpendicular magnetic field, the gaps close and reopen with an appropriate hopping parameter²⁵. The experimental realization of topological transition and its precise and flexible control have the potential to extend functionalities for practical applications which utilize the topological edge states^{17,26–30}. However, it is challenging to widely tune the hopping parameters experimentally once the systems are fabricated. In several previous works, topological phase transitions of electric circuits have been experimentally observed including variable capacitors^{31–33}, but the phase transition is limited to a binary fashion i.e., it occurs between topological and trivial phases.

Here, we observe the bulk-edge correspondence in topological pumping by implementing the classical analog of the quantum Hall phase and the topological phase transition in a one-dimensional electric circuit lattice. The topological phases and the transition are realized by accurately tuning the capacitances of variable capacitors. In the electric circuit lattice, eigenvalues and the local density of states are evaluated by measuring impedance spectra at nodes of the lattice. The topological numbers of the

edge states are determined by their locations (left- or right-edge), where the change of the location occurs associated with the topological transition. The bulk Chern numbers are extracted by using the Středa's formula in the mappings of impedance spectra, which show fractal patterns of the Hofstadter butterfly. Although peaks in the impedance spectra have finite bandwidths and some of the peaks are overlapped due to the loss of the circuit, the number of the eigenvalues is successfully counted by fitting the experimental spectra by using the Lorentzian function.

Results

Electric LC resonators to emulate the Harper-Hofstadter-Hatsugai model. The features of two-dimensional electrons on a square lattice in a magnetic field with NN (t_a and t_b in x - and y -directions, respectively) and NNN (t_c) hoppings, called the Harper-Hofstadter-Hatsugai (HHH) model^{25,34}, can be implemented as a one-dimensional system through the dimensional reduction^{25,34}, that is, one of the components of the two-dimensional momentum is replaced with cyclic time. We show that the classical analog of the HHH model can be synthesized in a tunable one-dimensional electric circuit by modulating capacitances or inductances appropriately.

Here, we consider a lossless electric circuit consisting of N nodes and the corresponding LC resonators, where neighboring LC resonators are coupled. According to Kirchhoff's law, the current \mathbf{I} and the voltage \mathbf{V} satisfy^{23,35}

$$\mathbf{I} = \left(i\omega C + \frac{1}{i\omega} W \right) \mathbf{V}, \quad (1)$$

where C and W are the $N \times N$ matrices of capacitances and the inverse of inductances of the circuit, and \mathbf{I} and \mathbf{V} are the N -vectors. ω is the angular frequency of alternating current. The HHH model can be implemented in either of the two cases; the first case has a fixed inductance and various capacitances of the circuit, and the second case has a fixed capacitance and various inductances. Here, we select the first case for the use of the advantages of variable capacitors that have been widely used in electric circuits, as shown in Fig. 1a, i.e., the system of Fig. 1a consists of N nodes and the corresponding resonators with each resonator having a constant inductance L_0 and a variable capacitance C_j ($1 \leq j \leq N$). The neighboring j th and $(j+1)$ th resonators are capacitively coupled by the capacitance C_{j+1} . $C_{0,1}$ is the capacitance between node 1 and the ground through jumper 2. In the periodic boundary condition (PBC), jumper 1 has the short connection with jumpers 2 and 3 being opened. Likewise, in the open boundary condition (OBC), jumpers 2 and 3 have the short connections with jumper 1 being opened.

Under the constant inductance L_0 , Eq. (1) is then rewritten as

$$\mathbf{I} = i\omega C_0 \left[H - \frac{\omega_0^2}{\omega^2} E \right] \mathbf{V}, \quad (2)$$

where

$$H = \frac{1}{C_0} \begin{bmatrix} C_1 + C_{0,1} + C_{1,2} & -C_{1,2} & 0 & \dots & 0 & -DC_{N,N+1} \\ -C_{1,2} & C_2 + C_{1,2} + C_{2,3} & -C_{2,3} & \dots & \dots & 0 \\ 0 & -C_{2,3} & \ddots & \dots & \dots & \dots \\ \vdots & 0 & \vdots & \ddots & \dots & \dots \\ 0 & \vdots & \vdots & \vdots & \ddots & -C_{N-1,N} \\ -DC_{N,N+1} & \vdots & \vdots & \vdots & -C_{N-1,N} & C_N + C_{N-1,N} + C_{N,N+1} \end{bmatrix}, \quad (3)$$

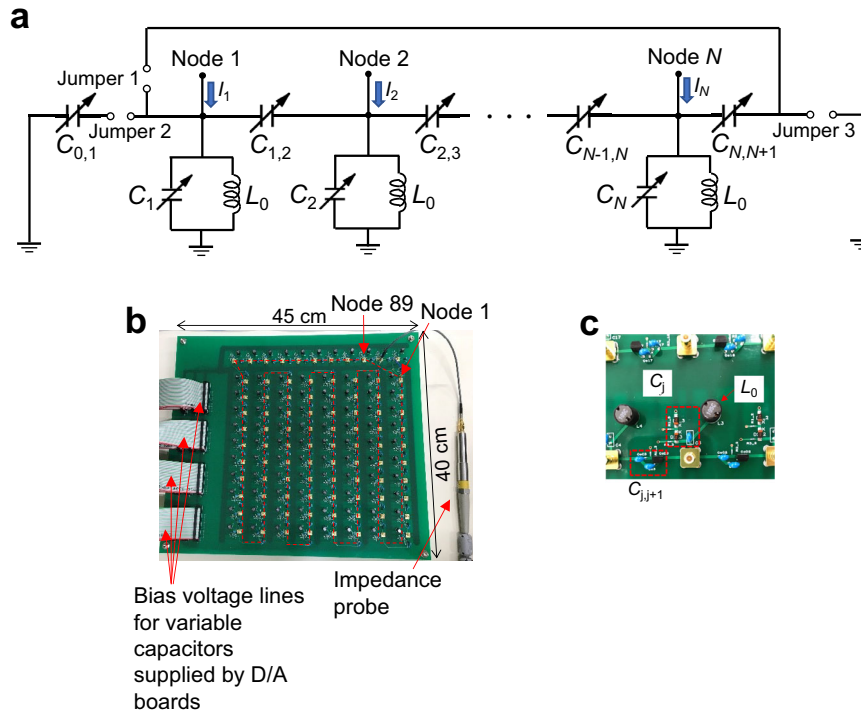


Fig. 1 Circuit platform for emulating the Harper-Hofstadter-Hatsugai (HHH) model. **a** Circuit diagram consisting of $N = 89$ LC resonators with neighboring resonators being coupled capacitively. N , L_0 , C_j , $C_{j,j+1}$, and I_n are the number of LC resonators, the inductance of the inductors, the capacitance of the j th LC resonator, the capacitance between the j th and the $(j+1)$ th nodes, and the current flowing into node n from outside of the node, respectively. The periodic boundary condition (PBC) is imposed by having jumper 1 to be short connection with jumpers 2 and 3 being opened. Likewise, the open boundary condition (OBC) is imposed by having jumpers 2 and 3 be short connections with jumper 1 being opened. **b** Fabricated circuit. LC resonators are coupled in series, which is indicated by the dashed line. The capacitances of variable capacitors were controlled by DC bias voltages supplied from the multi-channel D/A boards. The circuit system is implemented on a 40 cm \times 45 cm FR4 board. The top layer of the circuit board contains signal lines and circuit components. The bottom layer has the ground plane and bias voltage lines for the control of variable capacitors. The impedance probe is connected to a node by using a coaxial cable. **c** Unit cell of the circuit. Wire-wound inductors, ceramic capacitors, and variable capacitors are mounted. Each LC resonator has a node connector to measure the impedance between the corresponding node and the ground.

and $\omega_0 = 1/\sqrt{L_0 C_0}$. (We have normalized the matrix H by the capacitance C_0 .) E is the identity matrix. The boundary condition is periodic (open) when $D = 1$ ($D = 0$). Note that $C_{0,1} + C_{N,N+1}$ holds when imposing the PBC. We set the capacitances in the diagonal and non-zero off-diagonal components so that they satisfy $(C_j + C_{j-1,j} + C_{j,j+1})/C_0 = -2t_a \cos(\frac{2\pi}{T}\tau + 2\pi\phi_j) + \text{const.}$ and $C_{j,j+1}/C_0 = -t_b \{1 - 2t_c \cos(\frac{2\pi}{T}\tau + 2\pi\phi_j + \pi\phi)\}$, respectively, to emulate the HHH model. Here, *const.* stands for an offset value for those capacitances to be positive. The parameters τ , T , ϕ , and t_c are the adiabatic parameter (regarded as time variable^{10,14}), the period of the adiabatic parameter, the magnetic flux, and the NNN hopping amplitude normalized by t_b ($t_c = t_c'/t_b$), respectively.

In an electric circuit, the local density of states in quantum systems is evaluated by measuring the real part of the impedance at node n with other nodes being opened. The real part of the impedance at n node Z_n is expressed as²¹

$$\text{Re}[Z_n(\omega + i0)] = \frac{1}{2fC_0} \sum_i \delta\left(\lambda_i^H - \frac{\omega_0^2}{\omega^2}\right) |\psi_{i,n}|^2, \quad (4)$$

where λ_i^H and $\psi_{i,n}$ are the eigenvalue and the n th component of the i th eigenmode of H , respectively. f is the frequency $\omega/2\pi$. The detail of the derivation of Eq. (4) is described in Supplementary Note 4.

Figure 1b, c shows the top view and the unit cell of the fabricated circuit. Wire-wound inductors, ceramic capacitors, and variable capacitors are mounted on a FR4 board, and $N = 89$ LC

resonators are coupled in series (represented by the red dashed line). The capacitances are tuned by DC bias voltages supplied from the multi-channel digital to analog (D/A) converter boards, so that the capacitances are distributed to emulate the HHH model.

Observation of edge states near the topological phase transition.

We now turn to our experimental results. As shown above, the local density of states at node n is evaluated by measuring the impedance at the node. In order to observe spectra for the bulk and topological edge states, we select nodes 1, 44, 45, and 89 for measuring the impedances, where we assume that nodes 1 and 89 correspond to the left-edge and the right-edge, respectively, and the average of the impedances at nodes 44 and 45 correspond to the bulk. We vary τ from 0 to 1 with $\phi = 1/2$ fixed in the OBC. First, we set the NNN hopping parameter as $t_c = 0.1$. Figure 2a–c show the impedance maps of the bulk, the left-edge, and the right-edge, respectively. We observe the gap around $0.96(\omega_0/\omega)^2$ in the bulk (white horizontal dashed line, Fig. 2a). On the other hand, there are states at $\tau = 0.75$ for the left-edge (Fig. 2b) and at $\tau = 0.25$ for the right-edge (Fig. 2c) at $0.96(\omega_0/\omega)^2$ (white horizontal dashed line, Fig. 2b, c), respectively. Figure 2d shows the impedance spectra of the three cases at $\tau = 0.25$. We clearly observe the strong peak in the impedance of the right-edge and small impedances of the left-edge and the bulk at $0.96(\omega_0/\omega)^2$. Similarly, for $\tau = 0.75$, there is the strong peak in the impedance of the left-edge and small impedances of the right-edge and the bulk at the same frequency ($\tau = 0.75$ in Fig. 2a–c). Therefore, we

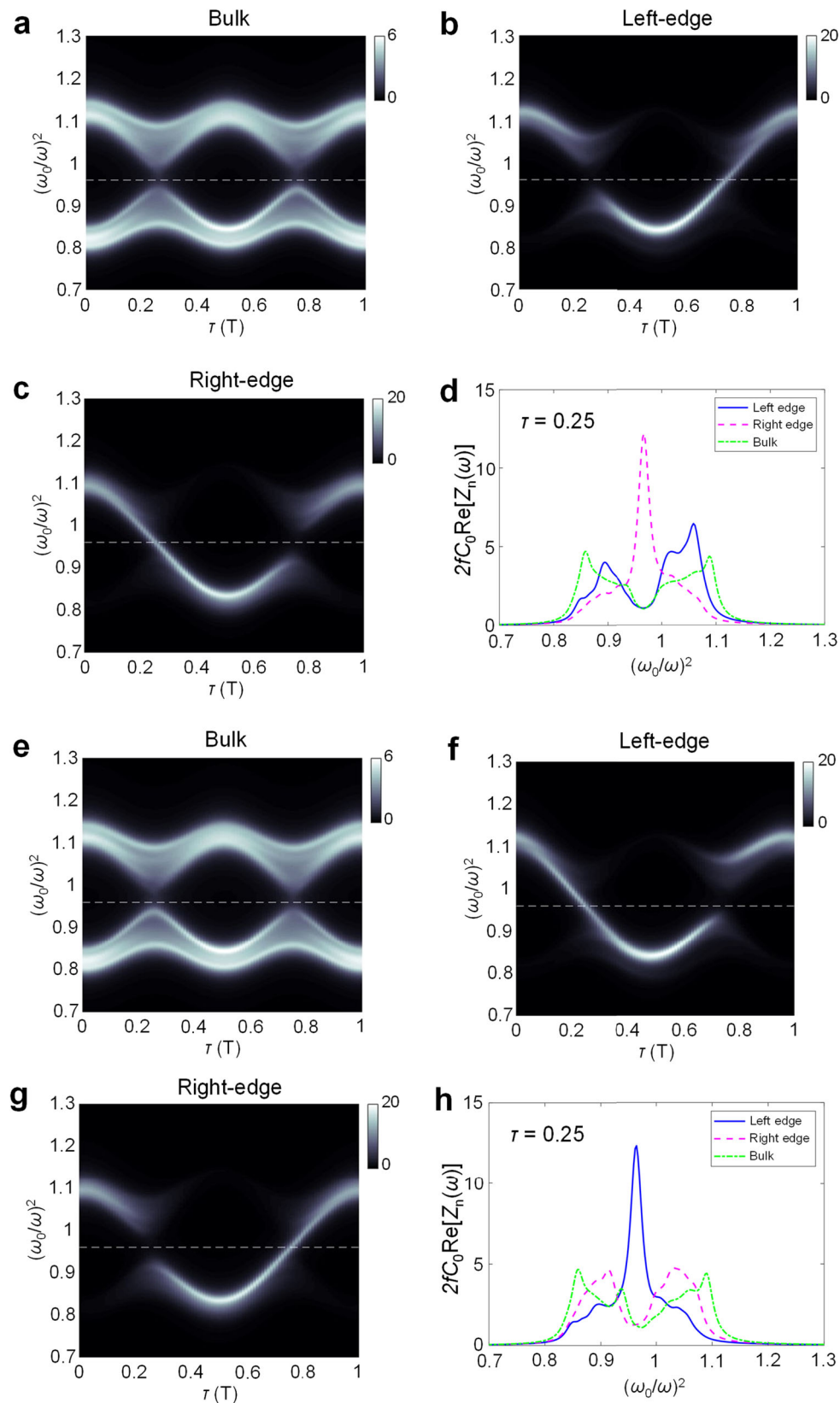


Fig. 2 Experimentally observed topological edge states near the topological transition at a flux parameter of $\phi = 1/2$. **a–c** Impedance maps in the τ - $(\omega_0/\omega)^2$ space for $t_c = 0.1$, where τ , ω_0 , ω , and t_c are the adiabatic parameter, the normalizing angular frequency, the angular frequency, and the next-nearest-neighbor hopping parameter, respectively. **d** Impedance spectra for $t_c = 0.1$ and $\tau = 0.25$. **e–g** Impedance maps for $t_c = -0.1$. **h** Impedance spectra for $t_c = -0.1$ and $\tau = 0.25$. In **a**, **e**, the averages of nodes 44 and 45 (bulk, the color bars show $2fC_0\text{Re}\{[Z_{44}(\omega) + Z_{45}(\omega)]/2\}$) are shown, where f , C_0 and $Z_n(\omega)$ are the frequency, the normalizing capacitance and the impedance at ω on node n . **b**, **f** show impedance maps on node 1 (left-edge, the color bars show $2fC_0\text{Re}[Z_1(\omega)]$). **c**, **g** Show impedance maps on node 89 (right edge, the color bars show $2fC_0\text{Re}[Z_{89}(\omega)]$). The dashed lines in **a–c** and **e–g** are the pseudo-Fermi energy.

conclude that the left- and right-edge states are observed at $\tau = 0.75$ and $\tau = 0.25$, respectively.

The topological phase transition implies the change of the behaviors of edge states. To see this, we invert the sign of t_c as $0.1 \rightarrow -0.1$. The results are shown in Fig. 2e–g. As in the case of $t_c = 0.1$, we observe the gap around $0.96(\omega_0/\omega)^2$ in the bulk [white horizontal dashed line, (Fig. 2e)]. Contrary to the case of $t_c = 0.1$, there are states at $\tau = 0.25$ for the left-edge (Fig. 2f) and at $\tau = 0.75$ for the right-edge (Fig. 2g) at $0.96(\omega_0/\omega)^2$ (white horizontal dashed line, Fig. 2f, g), respectively. Figure 2h shows the impedance spectra of the three cases at $\tau = 0.25$. We clearly observe the strong peak in the impedance of the left-edge state and small impedances of the right-edge state and the bulk state. Thus, the left- and right- edge states are observed at $\tau = 0.25$ and $\tau = 0.75$, respectively. This means that the locations of edge states have flipped by the topological transition from $t_c = 0.1$ to -0.1 .

Here, we deduce the topological numbers of the edge states I_{edge} . We assume the “virtual Fermi energy” in the gap of $0.96(\omega_0/\omega)^2$ (white horizontal dashed line, Fig. 2a–c, e–g). In the case of $t_c = 0.1$, as τ increases, eigenvalues of the right-edge state decrease across the virtual Fermi energy at $\tau = 0.25$, i.e., the right-edge state becomes occupied. Likewise, eigenvalues of the left-edge state increase across the virtual Fermi energy at $\tau = 0.75$, i.e., the right-edge state becomes unoccupied. According to the theory of the topological pumping¹³, $I_{\text{edge}} = 1$ is determined from the edge state for the case of $t_c = 0.1$. On the contrary, the left-edge state becomes occupied at $\tau = 0.25$ and the right-edge state becomes unoccupied at $\tau = 0.75$ when t_c is inverted as $0.1 \rightarrow -0.1$. Thus, $I_{\text{edge}} = -1$ is determined for the case $t_c = -0.1$.

We note that our result is consistent with the behavior of the massive Dirac fermion³⁶. Theoretically, the edge state has a linear dispersion in a bulk gap when the gap is opened, which is the feature of the massive Dirac fermion^{36–38}. The similar feature is observed in our experiment. The edge states in our experiment have approximately linear dispersions crossing the virtual Fermi energy, and the sign of the derivative of the dispersions on τ at the same node is inverted in the topological transition.

Observation of bulk Chern numbers in the topological phase transition. In the previous section, we observed the topological phase transition by the edge states under the OBC. Here we extract the bulk Chern numbers from experimental impedance spectra of the Hofstadter butterfly under the PBC by employing Středa’s formula. We will show that the bulk Chern numbers are consistent with topological numbers obtained from the edge states.

We vary the flux parameter $\phi = p/q$, where the integer p is varied from 1 to 88 with $q = 89$ fixed. For each p , impedance spectra for all $N = 89$ nodes are measured. The details of the measurements are presented in Methods. We have experimentally measured the impedance spectra $2fC_0 \sum_{n=1}^{89} \text{Re}[Z_n(\omega)]$. The impedance spectra for all p values are mapped in Fig. 3a, c, e for $t_c = 0, 0.1$, and -0.1 , respectively. Clear contrast of high impedance (bright color) to low impedance (dark color) is observed even in regions of higher-order gaps of the Hofstadter butterfly spectra. In the case of $t_c = 0$, the Hofstadter butterfly map is symmetric with respect to $\phi = 1/2$. In the case of $t_c = 0.1$, the center gap opens at $\phi = 1/2$ and the large gap runs from the left to the right upwards (Fig. 3c). When the sign of the t_c is inverted, the connection of the center gap of the Hofstadter butterfly switches and the large gap runs from the left to the right downwards (Fig. 3e). The butterfly spectra are well reproduced by numerical calculations and the circuit simulations (see Supplementary Note 2).

To extract the bulk Chern number C_{bulk} , we employ the Středa’s formula³⁹, $\Delta \text{IDS} / \Delta \phi = C_{\text{bulk}}$, where IDS represents the integrated density of states which is the number of eigenvalues below the target gap divided by the total number of eigenvalues. For the lossless case, each eigenstate, in principle, appears as a peak in the impedance spectrum. However, in the presence of resistive loss, some of the eigenstates having a finite bandwidth are overlapped in a peak of the impedance. In order to count the number of eigenstates, we fit the spectra of $2fC_0 \sum_{n=1}^{89} \text{Re}[Z_n(\omega)]$ by using the Lorentzian function of $\sum_i A_i \frac{a_i}{\pi^2 [(\omega_0/\omega)^2 - (\omega_0/\omega_i)^2]^2 + a_i^2}$ where A_i , a_i ,

and ω_i represent the area of the Lorentzian, the half width at half maximum, and the peak angular frequency ω_i of the i th peak. Thus, the number of eigenstates in a peak is counted by A_i even when some of those eigenstates are overlapped or degenerated. Therefore, $\sum_i A_i / \sum_i A_i$ equivalently corresponds to the IDS, where Σ' indicates the summation below the gap we consider. Examples of the approximated spectra are shown in the Supplementary Note 3. The least square method was used for the approximation of the Lorentzian curves, where the number and positions of spectral peaks are determined by the function *findpeaks* of MATLAB⁴⁰ with A_i and a_i being fitting parameters. First, we verify the derivation of bulk Chern numbers in the specific gaps of the butterfly using $t_c = 0$, which are indicated by labels in Fig. 3a. The ϕ dependence of $\sum_i A_i / \sum_i A_i$ below the target gaps is shown in the top panel of Fig. 3b. The bottom panel of Fig. 3b shows the residual of the approximation mentioned above, where the residual is calculated by integrating the deviation of the fitting curve from the experimental curve along $(\omega_0/\omega)^2$ with respect to the corresponding experimental area for each ϕ . In Fig. 3b, we observe that $\sum_i A_i / \sum_i A_i$ exhibits a symmetric set of linear lines over the range of ϕ . This is the Wannier diagram⁴¹ and its global features are reproduced experimentally. Table 1 shows the summary of measured $\frac{\Delta}{\Delta \phi} (\Sigma' A_i / \Sigma A_i)$ for each gap, where $\Delta \phi = 1/89$. We have retrieved the experimental values using linear functions from the hatched range of ϕ ($5/89 \leq \phi \leq 16/89, 73/89 \leq \phi \leq 85/89$), where the residual of the spectra approximation is less than 0.05 (bottom panel of Fig. 2b). The experimental values (the 2nd row in Table 1) are almost integers for the gaps, which are consistent with the theoretical values²⁵ (the 3rd row in Table 1). Therefore, deducing Chern numbers up to ± 3 is confirmed. The deviation of the experimental values from the theoretical values may attribute to the accuracy of the accumulation $\Sigma' A_i$ below the gap, i.e., high accuracy is obtained when the target gaps are located below $0.96(\omega_0/\omega)^2$ (the subscripts of labels are b and c) for Chern numbers of $\pm 1, \pm 1, \pm 2$, and ± 3 . We note that the residual is not small out of the hatched range of ϕ [bottom panel of Fig. 2b]. This can be related to the number of spectral peaks in the Lorentzian approximation. Namely, within the hatched region, e.g., at $\phi = 10/89$, the Lorentzian approximation has 9 peaks, and excellently agrees with the experimental spectrum (See Supplementary Fig. 3a). On the other hand, at $\phi = 30/89$, which is out of the hatched region, the Lorentzian approximation has only 3 peaks, and the discrepancy of the approximation curve from the experimental curve in the spectrum is pronounced (See Supplementary Fig. 3c).

Next, we deduced the bulk Chern number of the center gap across $\phi = 1/2$ for the cases of $t_c = \pm 0.1$. Figure 3d, f shows the corresponding $\frac{\Delta}{\Delta \phi} (\Sigma' A_i / \Sigma A_i)$ as a function of ϕ below the center gap. The slopes of the linearly approximated line in the hatched ranges are deduced to be 1.02 ($6/89 \leq \phi \leq 12/89$) and 1.21 ($76/89 \leq \phi \leq 84/89$) for $t_c = 0.1$ (Fig. 3d), and -1.23 ($4/89 \leq \phi \leq 13/89$) and -1.03 ($74/89 \leq \phi \leq 84/89$) for $t_c = -0.1$

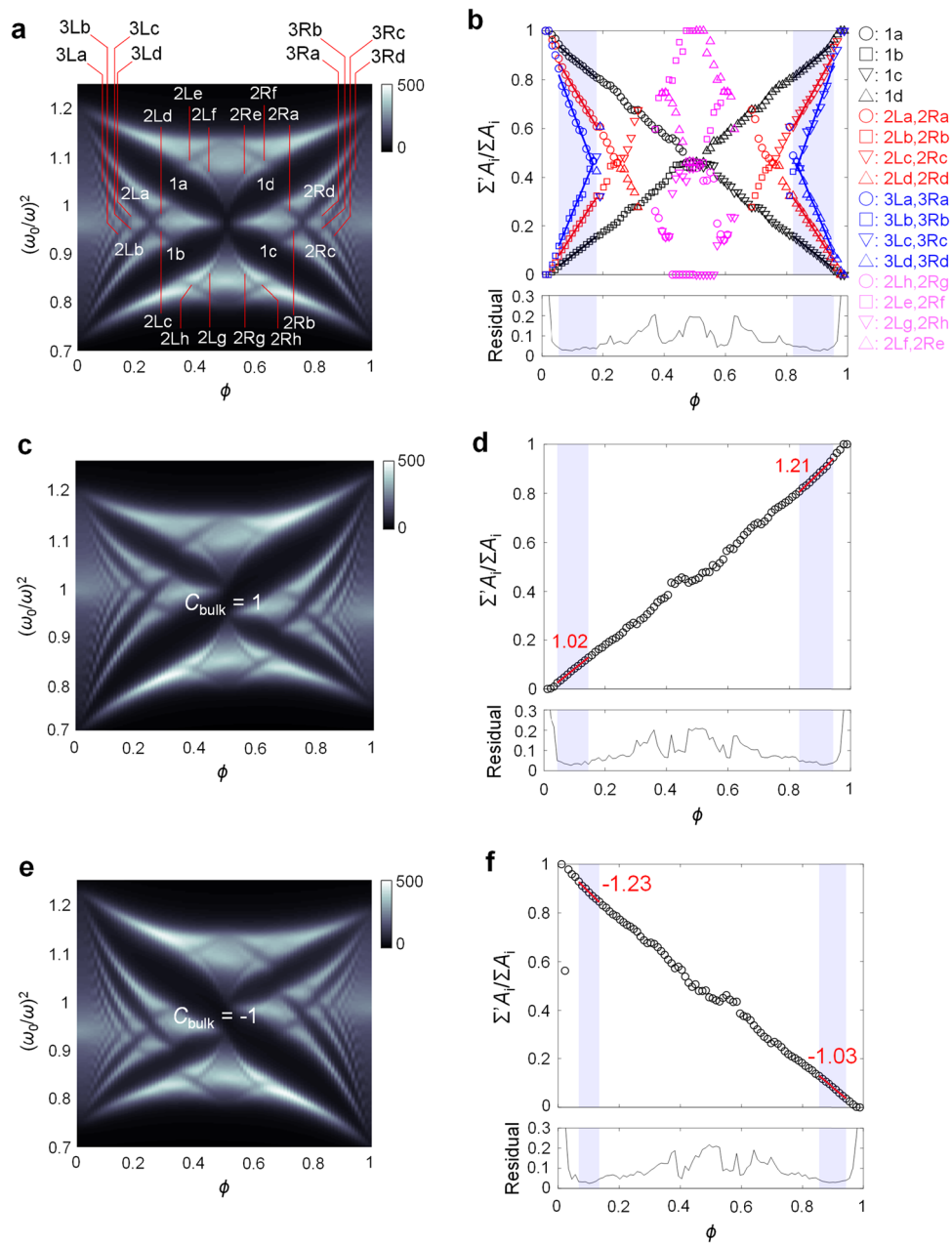


Fig. 3 Experimental observation of bulk Chern numbers in the topological phase transition. **a** Impedance maps as functions of $(\omega_0/\omega)^2$ and ϕ for $t_c = 0$, where ω_0 , ω , ϕ , and t_c are the normalizing angular frequency, the angular frequency, the flux parameter, and the next-nearest-neighbor hopping parameter, respectively. **b** $\sum_i A_i / \sum_i \Sigma_i A_i$ as a function of ϕ for $t_c = 0$, where Σ_i and A_i are the summation below the gap we consider and the area of the i th Lorentzian, respectively. **c** Impedance map for $t_c = -0.1$. **d** $\sum_i A_i / \sum_i \Sigma_i A_i$ as a function of ϕ for $t_c = 0.1$. **e** Impedance map for $t_c = -0.1$. **f** $\sum_i A_i / \sum_i \Sigma_i A_i$ as a function of ϕ for $t_c = -0.1$. In **a**, **c**, **e**, the color bars show $2fC_0 \sum_{n=1}^{89} \text{Re}[Z_n(\omega)]$, where f , C_0 and $Z_n(\omega)$ are the frequency, the normalizing capacitance, and the impedance at ω on node n . The label in each of the maps in **c**, **e** represents the Chern number of the gap determined from **d**, **f**. Each value of $\sum_i A_i / \sum_i \Sigma_i A_i$ in **d** and **f** is obtained by the linear approximation from the corresponding hatched range of ϕ .

Table 1 Measured $\frac{\Delta}{\Delta\phi} \left(\frac{\sum_i A_i}{\sum_i \Sigma_i A_i} \right)$ for each gap.

Labels of gaps	1a	1b	1c	1d	2La	2Lb	2Rc	2Rd	3La	3Lb	3Rc	3Rd
$\frac{\Delta}{\Delta\phi} \left(\frac{\sum_i A_i}{\sum_i \Sigma_i A_i} \right)$	-1.06	0.99	-1.01	1.09	-2.13	1.96	-1.96	2.24	-3.27	3.03	-3.04	3.51
Theoretical Chern numbers ²⁵	-1	1	-1	1	-2	2	-2	2	-3	3	-3	3

Σ_i , A_i , and ϕ are the summation below the gap we consider, the area of the i th Lorentzian and the flux parameter, respectively. Those values are obtained from the hatched regions ($5/89 \leq \phi \leq 16/89, 73/89 \leq \phi \leq 85/89$) in Fig. 3b.

(Fig. 3f), respectively, resulting in bulk Chern numbers of the center gap 1 and -1 . The bulk Chern numbers are consistent with the topological numbers of the edge states, i.e., $C_{\text{bulk}} = I_{\text{edge}}$. Therefore, we have experimentally confirmed the bulk-edge correspondence. In Ref. ²⁵, bulk Chern numbers were theoretically obtained, and our results are consistent with the theoretical results.

Discussion

Here we compare our results with those for the other artificial topological systems. Although the bulk Chern numbers in cold atom systems have been measured by using optical lattices^{11,12,42,43}, the measurement of the corresponding edge state is hindered since a harmonic trap makes it difficult to define the edge in such systems. In another class of topological systems, the winding number and the corresponding edge state in one-dimensional split-ring resonators⁴⁴ and a thermal lattice system^{45,46} have been measured. Our study is distinctively different from Ref. ^{44,45} in that the topological number we observed is the Chern number, while the topological phase discussed in Ref. ^{44,45} based on Su-Schrieffer-Heeger model which has one-dimensional chiral symmetry protected topological phase. Both bulk Chern numbers and the corresponding edge states are measured for the first time in our system.

In our system under the OBC, the edge states have been observed from the impedance maps as functions of $(\omega_0/\omega)^2$ and τ (Figs. 2a–c, e–g). Our circuit system provides highly efficient measurement process. Namely, in the previous systems^{15,47}, parameters are changed by hands or other means thus it may take days to obtain a single adiabatic cycle. On the other hand, the parameter tuning in our system is accomplished by only adjusting the DC bias voltages on the variable capacitors. The subsequent measurement of the spectra is automatically controlled in our system, which enables us to obtain the spectrum accurately and efficiently. Our electric circuit is a promising platform to investigate adiabatic behaviors of large-scale topological systems.

Our electric circuit system is also an effective platform that enables the experimental study of the nature of the Hofstadter butterfly. Although the Hofstadter butterfly spectrum is the characteristic feature of the energy spectrum of electrons on a square lattice⁴⁸, its strong magnetic field is unrealistic for two-dimensional electrons in solid. Recently, the Hofstadter butterfly spectra have been observed experimentally using microwave⁴⁹, acoustic⁵⁰, optical resonators⁵¹, superconducting q-bits⁵², and graphene superlattices^{53–55}. As for the resolution of the butterfly, for instance, up to the third-order fractal patterns have been observed using coupled acoustic resonators in Ref. ¹⁵. In our electric circuit system, we have clearly observed up to the fourth-order butterflies on the right and left sides as well as the second-order butterflies in upper and lower half, indicating the advantage of the electric circuits in terms of resolution. In addition, the evolution of the Hofstadter butterfly by changing the NNN hopping parameter²⁵ is experimentally observed for the first time.

Besides the framework employed in this work, the band structure has also been discussed for the admittance spectrum of electric circuits^{35,56,57}, where eigenvalues are obtained by voltage response of all nodes to a fixed local current input at a fixed frequency. In this work, we rather adopted the impedance measurements than admittance eigenvalue measurement because impedance spectra are easily measured by general-purpose equipment.

Beyond the fundamental study, our circuit scheme can trigger various applications of electric circuits, where topological stability is effectively utilized, because the LC resonator is a basic circuit

building block, for example, for wireless power transfer^{17,30}, oscillator⁵⁸, and circuit quantum electrodynamics devices⁵⁹.

Methods

Circuit elements. We used inductors 22R105C (Murata Manufacturing Co., Ltd.) with a measured inductance of 930 μH . Multilayer ceramic capacitors (RDE series, Murata Manufacturing Co., Ltd.) with measured capacitances of 470 pF and 9 pF are used for C_n and $C_{n,n+1}$ in parallel with variable capacitors (HVR100, Hitachi, Ltd. and 1SV101, Toshiba, Co. Ltd.), respectively. The capacitances of variable capacitors and the inductances with each series resistance of inductors are measured using a precision LCR meter (E4980A, Agilent). The dependencies of variable capacitors on DC bias voltages are shown in Supplementary Note 1.

Impedance measurements. Impedance spectra for the Hofstadter butterfly are measured at 89 points of τ with an equal interval of $2\pi\phi T$ using node 1. This corresponds to the measurements for all nodes, which saves time and effort to change the nodes. Multi-channel D/A converter boards (LF70, L and F, Inc.) and a CPU board (LF64, L and F, Inc.) are used to tune the capacitances of variable capacitors. DC bias voltages are supplied from six multi-channel D/A converter boards. Each board has 32 ch 12 bit D/A converters. The boards are controlled by a CPU board. The CPU board is controlled by using the LabView (National instruments). Tuning the capacitance and the corresponding frequency sweep of impedance measurement is automatically conducted using the laptop computer (see Supplementary Note 1). The impedance spectra are measured using an impedance analyzer (Agilent, 4294 A) with an impedance probe (42941 A). The impedance spectra are measured with an excitation voltage of 500 mV. We used $t_a = t_b = C_c/C_0$, and we set C_0 , C_c and $const.$ as 660 pF, 47 pF, and 1, respectively.

Circuit simulations. Electric circuit simulations, whose results are shown in Supplementary Note 2, are performed with LTspice⁶⁰. Considering the frequency dependence of the resistance of inductors, we use an equivalent series resistance of 15 Ω for the inductors. Impedance spectra are obtained by supplying an AC current source on the target node and measuring the voltage of the node using AC sweep analysis.

Data availability

The data that support the present study are available from the corresponding author upon reasonable request.

Code availability

LTspice and MATLAB codes used for the present study are available from the corresponding author upon reasonable request.

Received: 18 March 2022; Accepted: 27 June 2022;

Published online: 09 July 2022

References

- Thouless, D. J., Kohmoto, M., Nightingale, M. P. & den Nijs, M. Quantized hall conductance in a two-dimensional periodic potential. *Phys. Rev. Lett.* **49**, 405–408 (1982).
- Laughlin, R. B. Quantized Hall conductivity in two dimensions. *Phys. Rev. B* **23**, 5632–5633 (1981).
- Hasan, M. Z. & Kane, C. L. Colloquium: topological insulators. *Rev. Mod. Phys.* **82**, 3045–3067 (2010).
- Qi, X.-L. & Zhang, S.-C. Topological insulators and superconductors. *Rev. Mod. Phys.* **83**, 1057–1110 (2011).
- Halperin, B. I. Quantized hall conductance, current-carrying edge states, and the existence of extended states in a two-dimensional disordered potential. *Phys. Rev. B* **25**, 2185–2190 (1982).
- Hatsugai, Y. Edge states in the integer quantum Hall effect and the Riemann surface of the Bloch function. *Phys. Rev. B* **48**, 11851–11862 (1993).
- Klitzing, K., Dorda, G. & Pepper, M. New method for high-accuracy determination of the fine-structure constant based on quantized Hall resistance. *Phys. Rev. Lett.* **45**, 494–497 (1980).
- Kohmoto, M. Topological invariant and the quantization of the Hall conductance. *Ann. Phys.* **160**, 343–354 (1985).
- Hatsugai, Y. Chern number and edge states in the integer quantum Hall effect. *Phys. Rev. Lett.* **71**, 3697–3700 (1993).
- Thouless, D. Quantization of particle transport. *Phys. Rev. B* **27**, 6083–6087 (1983).

11. Lohse, M., Schweizer, C., Zilberberg, O., Aidelsburger, M. & Bloch, I. A thouless quantum pump with ultracold bosonic atoms in an optical superlattice. *Nat. Phys.* **12**, 350–354 (2015).
12. Nakajima, S. et al. Topological thouless pumping of ultracold fermions. *Nat. Phys.* **12**, 296–300 (2016).
13. Hatsugai, Y. & Fukui, T. Bulk-edge correspondence in topological pumping. *Phys. Rev. B* **94**, 041102(R) (2016).
14. Kraus, Y. E., Lahini, Y., Ringel, Z., Verbin, M. & Zilberberg, O. Topological states and adiabatic pumping in quasicrystals. *Phys. Rev. Lett.* **109**, 106402 (2012).
15. Ni, X. et al. Observation of Hofstadter butterfly and topological edge states in reconfigurable quasi-periodic acoustic crystals. *Commun. Phys.* **2**, 55 (2019).
16. Riva, E., Rosa, M. I. & Ruzzene, M. Edge states and topological pumping in stiffness-modulated elastic plates. *Phys. Rev. B* **101**, 094307 (2020).
17. Guo, Z., Jiang, H., Sun, Y., Li, Y. & Chen, H. Asymmetric topological edge states in a quasiperiodic Harper chain composed of split-ring resonators. *Opt. Lett.* **43**, 5142–5145 (2018).
18. Cheng, W., Prodan, E. & Prodan, C. Experimental demonstration of dynamic topological pumping across incommensurate bilayered acoustic metamaterials. *Phys. Rev. Lett.* **125**, 224301 (2020).
19. Grinberg, I. H. et al. Robust temporal pumping in a magneto-mechanical topological insulator. *Nat. Commun.* **11**, 1–9 (2020).
20. Ningyuan, J., Owens, C., Sommer, A., Schuster, D. & Simon, J. Time- and site-resolved dynamics in a topological circuit. *Phys. Rev. X* **5**, 021031 (2015).
21. Wang, Y., Price, H. M., Zhang, B. & Chong, Y. D. Circuit implementation of a four-dimensional topological insulator. *Nat. Commun.* **11**, 2356 (2020).
22. Zilberberg, O. et al. Photonic topological boundary pumping as a probe of 4D quantum Hall physics. *Nature* **553**, 59–62 (2018).
23. Imhof, S. et al. Topolectrical-circuit realization of topological corner modes. *Nat. Phys.* **14**, 925–929 (2018).
24. Kim, M., Jacob, Z. & Rho, J. Recent advances in 2D, 3D and higher-order topological photonics. *Light Sci. Appl.* **9**, 1–30 (2020).
25. Hatsugai, Y. & Kohmoto, M. Energy spectrum and the quantum Hall effect on the square lattice with next-nearest-neighbor hopping. *Phys. Rev. B* **42**, 8282–8294 (1990).
26. Ozawa, T. et al. Topological photonics. *Rev. Mod. Phys.* **91**, 015006 (2019).
27. Lu, L., Joannopoulos, J. D. & Soljačić, M. Topological photonics. *Nat. Photon.* **8**, 821–829 (2014).
28. Khanikaev, A. B. & Shvets, G. Two-dimensional topological photonics. *Nat. Photon.* **11**, 763–773 (2017).
29. Lan, C., Hu, G., Tang, L. & Yang, Y. Energy localization and topological protection of a locally resonant topological metamaterial for robust vibration energy harvesting. *J. Appl. Phys.* **129**, 184502 (2021).
30. Song, J. et al. Wireless power transfer via topological modes in dimer chains. *Phys. Rev. Appl.* **15**, 014009 (2021).
31. Serra-Garcia, M., Süsstrunk, R. & Huber, S. D. Observation of quadrupole transitions and edge mode topology in an LC circuit network. *Phys. Rev. B* **99**, 020304 (2019).
32. Hadad, Y., Soric, J. C., Khanikaev, A. B. & Alù, A. Self-induced topological protection in nonlinear circuit arrays. *Nat. Electron.* **1**, 178–182 (2018).
33. Zangeneh-Nejad, F. & Fleury, R. Nonlinear second-order topological insulators. *Phys. Rev. Lett.* **123**, 053902 (2019).
34. Kuno, Y. Disorder-induced chern insulator in the harper-hofstadter-hatsugai model. *Phys. Rev. B* **100**, 054108 (2019).
35. Lee, C. H. et al. Topolectrical circuits. *Commun. Phys.* **1**, 39 (2018).
36. Hatsugai, Y., Kohmoto, M. & Wu, Y.-S. Hidden massive dirac fermions in effective field theory for integral quantum Hall transitions. *Phys. Rev. B* **54**, 4898–4906 (1996).
37. Haldane, F. D. M. Model for a quantum Hall effect without Landau levels: condensed-matter realization of the “parity anomaly”. *Phys. Rev. Lett.* **61**, 2015–2018 (1988).
38. Semenoff, G. W. Condensed-matter simulation of a three-dimensional anomaly. *Phys. Rev. Lett.* **53**, 2449–2452 (1984).
39. Streda, P. Theory of quantised Hall conductivity in two dimensions. *J. Phys. C: Solid State Phys.* **15**, L717 (1982).
40. MathWorks. see <https://mathworks.com/help/matlab/> for “MathWorks, MATLAB R2019a”.
41. Wannier, G. A result not dependent on rationality for Bloch electrons in a magnetic field. *Phys. Status Solidi B* **88**, 757–765 (1978).
42. Aidelsburger, M. et al. Measuring the Chern number of Hofstadter bands with ultracold bosonic atoms. *Nat. Phys.* **11**, 162–166 (2014).
43. Asteria, L. et al. Measuring quantized circular dichroism in ultracold topological matter. *Nat. Phys.* **15**, 449–454 (2019).
44. Jiang, J. et al. Seeing topological winding number and band inversion in photonic dimer chain of split-ring resonators. *Phys. Rev. B* **101**, 165427 (2020).
45. Hu, H. et al. Observation of Topological Edge States in Thermal Diffusion. *Adv. Mater.* 2202257 (2022).
46. Yoshida, T. & Hatsugai, Y. Bulk-edge correspondence of classical diffusion phenomena. *Sci. Rep.* **11**, 1–7 (2021).
47. Apigo, D. J., Cheng, W., Dobiszewski, K. F., Prodan, E. & Prodan, C. Observation of topological edge modes in a quasiperiodic acoustic waveguide. *Phys. Rev. Lett.* **122**, 095501 (2019).
48. Hofstadter, D. R. Energy levels and wave functions of Bloch electrons in rational and irrational magnetic fields. *Phys. Rev. B* **14**, 2239–2249 (1976).
49. Kuhl, U. & Stockmann, H.-J. Microwave realization of the hofstadter butterfly. *Phys. Rev. Lett.* **80**, 3232 (1998).
50. Richoux, O. & Pagneux, V. Acoustic characterization of the Hofstadter butterfly with resonant scatters. *Europhys. Lett.* **59**, 34 (2002).
51. Zimmerling, T. J. & Van, V. Generation of Hofstadter’s butterfly spectrum using circular arrays of microring resonators. *Opt. Lett.* **45**, 714–717 (2020).
52. Roushan, P. et al. Spectroscopic signatures of localization with interacting photons in superconducting qubits. *Science* **358**, 1175–1179 (2017).
53. Dean, C. R. et al. Hofstadter’s butterfly and the fractal quantum Hall effect in moire superlattices. *Nature* **497**, 598–602 (2013).
54. Hunt, B. et al. Massive dirac fermions and hofstadter butterfly in a van der waals heterostructure. *Science* **340**, 1427 (2013).
55. Kumar, R. K. et al. High-order fractal states in graphene superlattices. *Proc. Natl. Acad. Sci. USA* **115**, 5135–5139 (2018).
56. Yoshida, T., Mizoguchi, T. & Hatsugai, Y. Mirror skin effect and its electric circuit simulation. *Phys. Rev. Res.* **2**, 022062(R) (2020).
57. Helbig, T. et al. Generalized bulk–boundary correspondence in non-Hermitian topolectrical circuits. *Nat. Phys.* **16**, 747–750 (2020).
58. Pozar, D. M. *Microwave Engineering*. John Wiley & sons (2011).
59. Tangpanitanon, J. et al. Topological pumping of photons in nonlinear resonator arrays. *Phys. Rev. Lett.* **117**, 213603 (2016).
60. Analog Devices. see <https://www.analog.com/en/design-center/design-tools-and-calculators/lts Spice-simulator.html> for “Analog devices, LTSpice XVII”.

Acknowledgements

This work is supported by JSPS KAKENHI Grants No. JP17H06138 (Y.H.), JP20H04627 (T.Y.), JP20K14371 (T.M.), JP21K13849 (Y.K.), JP21K13850 (T.Y.), JP22H05247 (T.Y.), and JST-CREST JPMJCR19T1(Y.H.).

Author contributions

K.Y. performed calculations, designed the measurement setup, and carried out the experiments. T.Y., T.M., Y.K., and Y.H. contributed to discussions on theoretical investigations. H.I. and Y.T. contributed to discussions on experimental investigations. All authors contributed to the manuscript preparation. Y.H. supervised the project.

Competing interests

The authors declare no competing interests.

Additional information

Supplementary information The online version contains supplementary material available at <https://doi.org/10.1038/s42005-022-00957-5>.

Correspondence and requests for materials should be addressed to Kenichi Yatsugi.

Peer review information *Communications Physics* thanks Xiang Ni and Romain Fleury for their contribution to the peer review of this work. Peer reviewer reports are available.

Reprints and permission information is available at <http://www.nature.com/reprints>

Publisher’s note Springer Nature remains neutral with regard to jurisdictional claims in published maps and institutional affiliations.



Open Access This article is licensed under a Creative Commons Attribution 4.0 International License, which permits use, sharing, adaptation, distribution and reproduction in any medium or format, as long as you give appropriate credit to the original author(s) and the source, provide a link to the Creative Commons license, and indicate if changes were made. The images or other third party material in this article are included in the article’s Creative Commons license, unless indicated otherwise in a credit line to the material. If material is not included in the article’s Creative Commons license and your intended use is not permitted by statutory regulation or exceeds the permitted use, you will need to obtain permission directly from the copyright holder. To view a copy of this license, visit <http://creativecommons.org/licenses/by/4.0/>.

© The Author(s) 2022